The Astrophysical Journal, 841:70 (10pp), 2017 June 1 https://doi.org/10.3847/1538-4357/aa709d

Variation of Supergranule Parameters with Solar Cycles: Results from Century-long Kodaikanal Digitized Ca II K Data

Subhamoy Chatterjee[1], Sudip Mandal[1], and Dipankar Banerjee[1,2]
[1] Indian Institute of Astrophysics, Koramangala, Bangalore 560034, India; dipu@iiap.res.in
[2] Center of Excellence in Space Sciences India, IISER Kolkata, Mohanpur 741246, West Bengal, India
Received 2017 February 9; revised 2017 April 26; accepted 2017 April 27; published 2017 May 25

Abstract

The Ca II K spectroheliograms spanning over a century (1907–2007) from Kodaikanal Solar Observatory, India, have recently been digitized and calibrated. Applying a fully automated algorithm (which includes contrast enhancement and the "Watershed method") to these data, we have identified the supergranules and calculated the associated parameters, such as scale, circularity, and fractal dimension. We have segregated the quiet and active regions and obtained the supergranule parameters separately for these two domains. In this way, we have isolated the effect of large-scale and small-scale magnetic fields on these structures and find a significantly different behavior of the supergranule parameters over solar cycles. These differences indicate intrinsic changes in the physical mechanism behind the generation and evolution of supergranules in the presence of small-scale and large-scale magnetic fields. This also highlights the need for further studies using solar dynamo theory along with magneto-convection models.

Key words: astronomical databases: miscellaneous – methods: data analysis – Sun: chromosphere – Sun: faculae, plages – Sun: granulation – techniques: image processing

1. Introduction

The Sun, a magnetically active star, has an atmosphere that varies widely with height in density and temperature. The lowermost layer of the atmosphere is known as the photopshere, where we observe the signature of solar convection, the granules (the characteristic scale of the granules is a few Mm). There are patterns on the solar surface that are larger (∼30 Mm) than the granular scales. These are known as supergranules. Supergranules appear in different shapes and sizes. The boundaries of these structures are the host of the magnetic fluxes, and the dispersal of this flux is believed to be governed by the diffusion that is caused by the evolution of the supergranules (Rast 2003; Crouch et al. 2007).

The origin of the supergranulation is not fully understood. It can be due to convection (like granules) or it can be a dynamic instability. The study of the supergranules is important because it reveals the intrinsic scale of the physical mechanism that drives these structures. Moreover, one can investigate the effect of a strong magnetic field by studying the supergranular properties separately for active and quite regions. There have been a few studies in the past on the detection and calculation of different properties of supergranules. Using an autocorrelation curve technique, Sýkora (1970) and Hagenaar et al. (1997) detected supergranular structures, whereas Muenzer et al. (1989) estimated the latitudinal dependence of the supergranule sizes by using Ca II images through a fast Fourier transform analysis for both active and quiet regions. These automated methods are useful in determining the aggregate properties of supergranules, but they fail to record the parameters of individual structures. In an another work, Berrilli et al. (1999) used an automated skeleton detection method and have shown the temporal variation of the quiet region cell size for one year data set. Hagenaar et al. (1997) showed the invariance of the supergranule scale distribution at different spatial smoothings. They also studied the distribution of supergranule scales and found that the scales are similar to Voronoi tessellation. A similar work has been made by Srikanth et al. (2000), who quantified the distribution using skewness and kurtosis parameters. In a recent work, McIntosh et al. (2011) explored the variation of the supergranular parameters from five independent sources using the "watershed segmentation" method to detect the supergranules in the images. From their results (for a period of 33 years, 1944–1976), they found imprints of the solar cycle variation in the supergranule parameters. Thus we see that a study of the supergranule parameters for several solar cycles is necessary to determine their relation with the large-scale solar variation.

Using the Kodaikanal digitized Ca II K data, we present for the first time the variation of the supergranular parameters for a period of 100 years (1907–2007) in this paper. Kodaikanal Solar Observatory (KSO) has archived 100 years (cycles 14–23) of chromospheric images in Ca II K (3933.67 Å) through an unchanged $f/21$ optics with a 30 cm objective. This gives an enormous opportunity to study the synoptic variation of supergranular cell sizes over many solar cycles and also to understand their correspondence with the solar activity. This paper is organized as follows: after presenting a brief data description in Section 2, we define the detection method and various parameters associated with supergranlues in Section 3. Results from the KSO are discussed in Section 4, whereas in Section 5 we present the results using the data from other observatories. Finally, Section 6 provides a brief summary and conclusion.

2. Data Description

The primary data used in this study are taken from the digitized archive of the Kodaikanal Ca II K observations[3] (Priyal et al. 2014; Chatterjee et al. 2016). In addition, we have also used data from the Precision Solar Photometric Telescope

[3] https://kso.iiap.res.in/data

Table 1
Details of the Different Data Sets Used in this Study

Data Source	Wavelength (passband) (Å)	Duration	Pixel Scale
KSO Ca II K	3933.67 (0.5)	1907–2007	0.″8
PSPT-ITALY	3934.00 (2.5)	1996–2016	1″
PSPT-USA	3934.00 (1.0)	2005–2015	1″

(PSPT) (Ermolli et al. 1998). The details of each data set are given in Table 1.

We used for comparison the V2.0 daily sunspot number data from the SIDC (Solar Influences Data Analysis Center), which are available at http://www.sidc.be/silso/datafiles.

3. Definitions and Methods

3.1. Detection of Supergranules

Supergranules are large-scale velocity structures with a spatial extent of ∼30 Mm and a typical lifetime of 25 hr (Rieutord & Rincon 2010). These structures also have a strong horizontal flow of ≈400 m s^{-1}. Now, in the intensity images taken through a chromospheric line such as Ca II K, we note a boundary-like pattern that is also known as the "chromospheric network." These networks outline the supergranular cells and can be used as a proxy for supergranular shape and size measurements (Simon & Leighton 1964). We follow this convention thoughout the paper. In order to identify these structures, we first select a rectangular region ("region of interest," ROI) at the disk center with sides equal to 60% of solar disk diameter. This selection is made in order to minimize the errors that are due to the projection effect. The different steps involved in detecting the supergranules from KSO and PSPT intensity images are shown in the different panels of Figure 1. We highlight the ROIs with rectangles, as shown in the 1(a) panels, and the full views of the ROIs are shown in the 1(b) panels. Next, these regions were histogram equalized and smoothed with a median filter to reduce noise (1(c) panels).

We used the morphological closing and subsequently watershed transform (Vincent & Soille 1991; Lin et al. 2003; McIntosh et al. 2011) on these ROI images to detect the supergranules. The basic principle behind the watershed transformation is as follows: when an image is visualized as a topographic surface with gray-levels as heights, watershed segmentation divides the image into catchment basins. All pixels corresponding to a basin are connected to a local minimum that falls within the basin through a pixel path of steadily decreasing intensity height (Sonka et al. 2014). Now, the rationale behind the usage of morphological closing was to avoid oversegmentation into smaller scales through the watershed method. The results of the watershed transformation on the ROI images are shown in the 1(d) panels. To visually check for the detection accuracy, we overplot the detected supergranular boundaries on the histogram-equalized images as shown in the 1(e) panels and find a very good match between the two. We also provide magnified 400″ × 400″ views of the 1(e) panels in the 1(f) panels to depict the overlap of network with the watershed boundaries (shown as dark blue double lines). After detecting the supergranules from every image using this method, we now define some of the parameters associated with it in the next section.

3.2. Scale, Circularity, and Fractal Dimension of Supergranules

All the detected supergranules from every single image were isolated using the region-labeling method (Sonka et al. 2014). To calculate the supergranulation scale (characteristic scale of these structures), we equate each supergranule area to the area of a circle, and the radius of this circle is defined as the supergranule scale. We take the average of these radii for each image to find a number called the average supergranule scale.

Next, we define the circularity of each supergranule by the expression $4\pi A/P^2$, where A and P denote the area and perimeter of each supergranule (Srikanth et al. 2000). In the digital domain, circularity shows some dependence on the size of the structures. This arises because the feature boundaries become exaggerated when size decreases (a result of the fixed pixel resolution). To correct for this dependency, we first calculate a trend of the circularity versus scale for each image by fitting a second-degree polynomial (Figure 2(a)), and then the data points are divided by the fitted curve to correct for the trend (Figure 2(b)). As larger areas are assumed to have correct (scale-independent) circularity, we multiplied the normalized circularity values by the minimum of the polynomial curve.

One of the other important parameters associated with a supergranule is the fractal dimension, which is a measure of the complexity and self-similarity of a structure (Mandelbrot 1982). It is also called fractional dimension, and it captures the dependence of structure details on scale. Now, the fractal dimension (D) is estimated from the area (A) and perimeter (P) of a given structure via the relation $P \propto A^{\frac{D}{2}}$ (Muller & Roudier 1994). Thus, twice the slope of the area versus perimeter plot, on a log-log scale, is equal to the fractal dimension (Paniveni et al. 2010).

4. Results from KSO

4.1. Full ROI; the Aggregate

As mentioned in the previous section, we calculated different supergranule parameters such as scale, circularity, and the fractal dimension within a selected ROI (we call it "aggregate" hereafter) from each of the KSO Ca II K images. Figure 3 shows the variation of the average supergranule scale over the nine cycles (cycles 14 to 22) studied in this paper. The green dots correspond to average scales determined from individual images, and the solid black curve represents a smoothed version of the same. We additionally plot the spline smoothed first and third quartile curves with blue and red dashes, respectively, in Figure 3, and this shows that the scatter in the data is smaller than the temporal variation of the parameter.

All the smoothed curves presented in this paper are generated using the CRAN package named "cobs" of the statistical analysis software R (details about this can be found in Feigelson & Babu 2012). This smoothing technique is based on basis splines (Reinsch 1967) and allows manual input features such as constraints and knot points. For this study we used a quadratic spline with the penalty parameter λ (Hastie & Tibshirani 1990) set to 1. This method takes care of the temporal variation of the data spread (or sudden discontinuities) and is effective in avoiding the "artificial" jitters as opposed to the conventional running-average technique. Moreover, to compare the two methods (spline smoothing and the

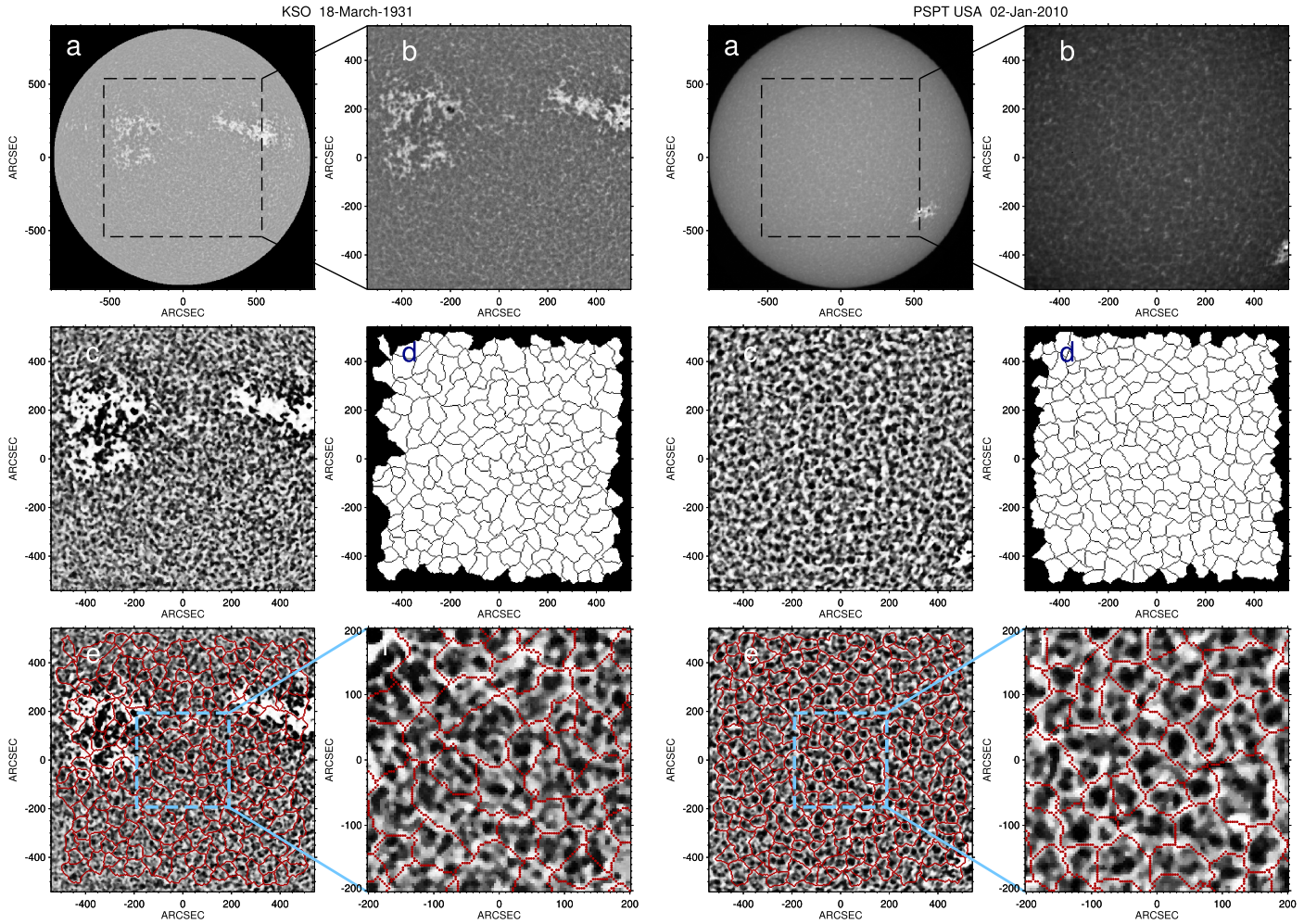

Figure 1. Different processing steps to detect supergranules. (a) Ca II K disk-centered image; (b) central window (as highlighted by the rectangle in (a)) used for further processing; (c) limb-darkening corrected, intensity-enhanced, and smoothed version of (b), (d) detected supergranules using the watershed transform (supergranule boundaries are shown in black); (e) supergranule boundaries from (d) overplotted on (c); and (f) magnified view of panel (e) with a FoV of $400'' \times 400''$.

running averaging), we repeated the entire presented analysis with running-averaged data, and the results are presented in the Appendix.

The vertical dashed line in Figure 3 indicates that the KSO image quality degraded substantially after this period (1997 onward/cycle 23 onward). Although we detected and calculated all the supergranule parameters also using the images from this time period (1997 onward, as shown in the plots), all the correlation values (with the SSN) were calculated for the period 1907–1996. To extend our analysis beyond 1996, we used the PSPT-Italy (1996–2016) and PSPT-USA (2005–2015) data to cover the remaining period, and the results from them are discussed in the subsequent sections.

Now from the curve we immediately note that it has a sunspot-cycle-like periodicity of ∼11 years. To understand its connection with the solar cycle more clearly, we overplot the smoothed sunspot number (SSN) data in the same panel (dashed curve). A positive correlation value of 0.76 confirms the in-phase variation of the average supergranule scale with the sunspot number. The calculated scale values (Figure 3) vary from 24 Mm (during the cycle minima) to 28–30 Mm (during the cycle maxima) with an average at around 26 Mm. These estimated scale values from the KSO data match the values presented in McIntosh et al. (2011) closely, where the authors used Mount Wilson Solar Observatory (MWO) historical data for three cycles (1944–1976). It must be emphasized here that McIntosh et al. (2011) could not obtain a clear trend of the in-phase variation of the supergranule radius with the SSN in all the three cycles they analyzed. In our analysis, when we look for the same period as presented in McIntosh et al. (2011), i.e., from 1944 to 1976, we note that the in-phase variation signature is prominently visible for all of the cycles. In fact, the one-to-one correlation with the SSN is clearly demonstrated for all the cycles (cycles 14–22) investigated in this study. Thus, we conclude that the long-term data availability at KSO has enabled us to establish the in-phase variation of the radius parameter with SSN over a much greater span of time than any other previous study.

4.2. Active and Quiet Regions

Since the main magnetic activities are concentrated on the active regions (ARs), it would be interesting to investigate the

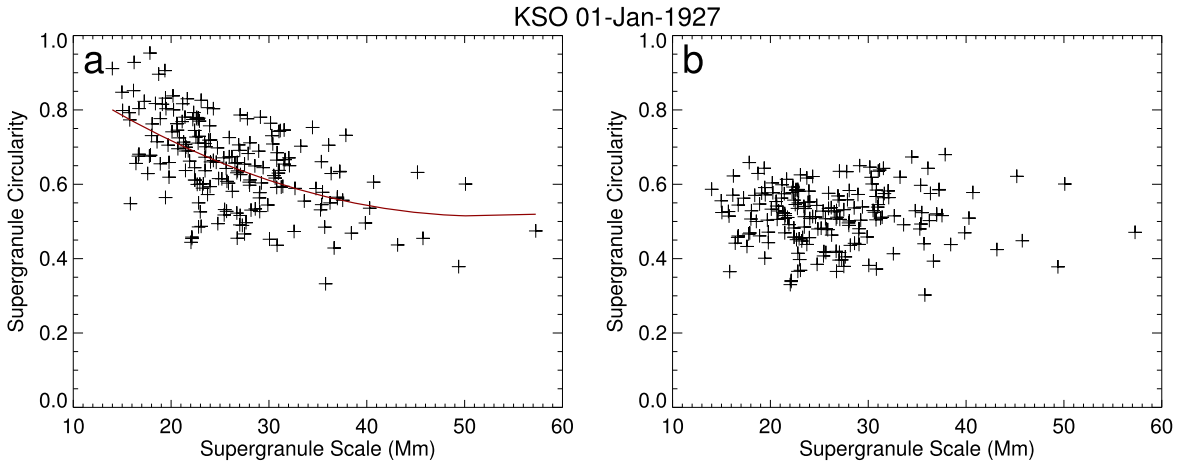

Figure 2. (a) Dependence of the supergranule circularity on the scale. The solid red line is the fitted second-degree polynomial on the observed trend; (b) the same as previously, only after removing the trend.

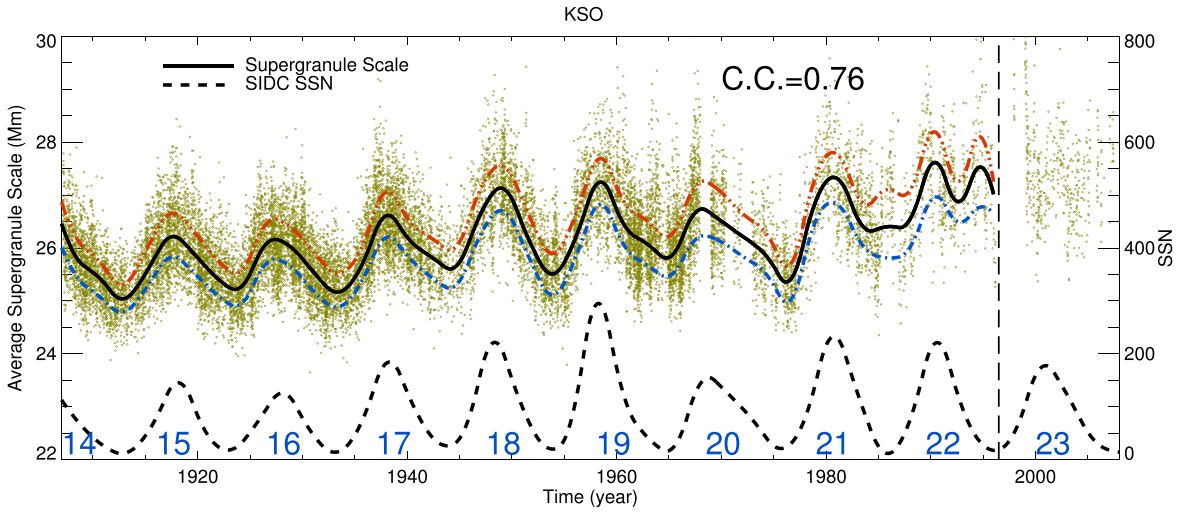

Figure 3. Cyclic variation of the mean supergranule scale for nine cycles. Green points correspond to data from the KSO. The black solid curve is the smoothed average supergranule scale. Blue and red dashed curves depict spline smoothing for the first and third quartiles, respectively. The black dashed curve depicts the temporal variation of the smoothed sunspot number (SSN). Cycle numbers are marked in blue.

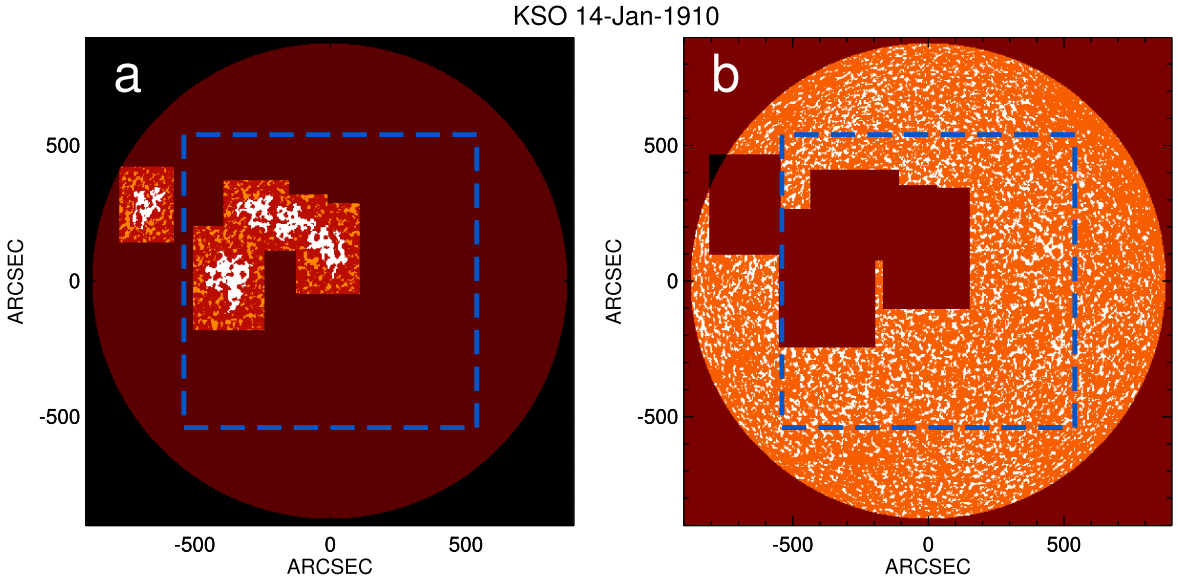

Figure 4. Separation of active and quiet region supergranules. (a) Rectangular regions with white plage structures are defined as active regions (ARs); (b) regions away from plage structures (outside the rectangular patches and inside the disk) are considered quiet regions (QRs). The dashed rectangles in both panels show the regions within which supergranule detection is performed (this is same as the ROI).

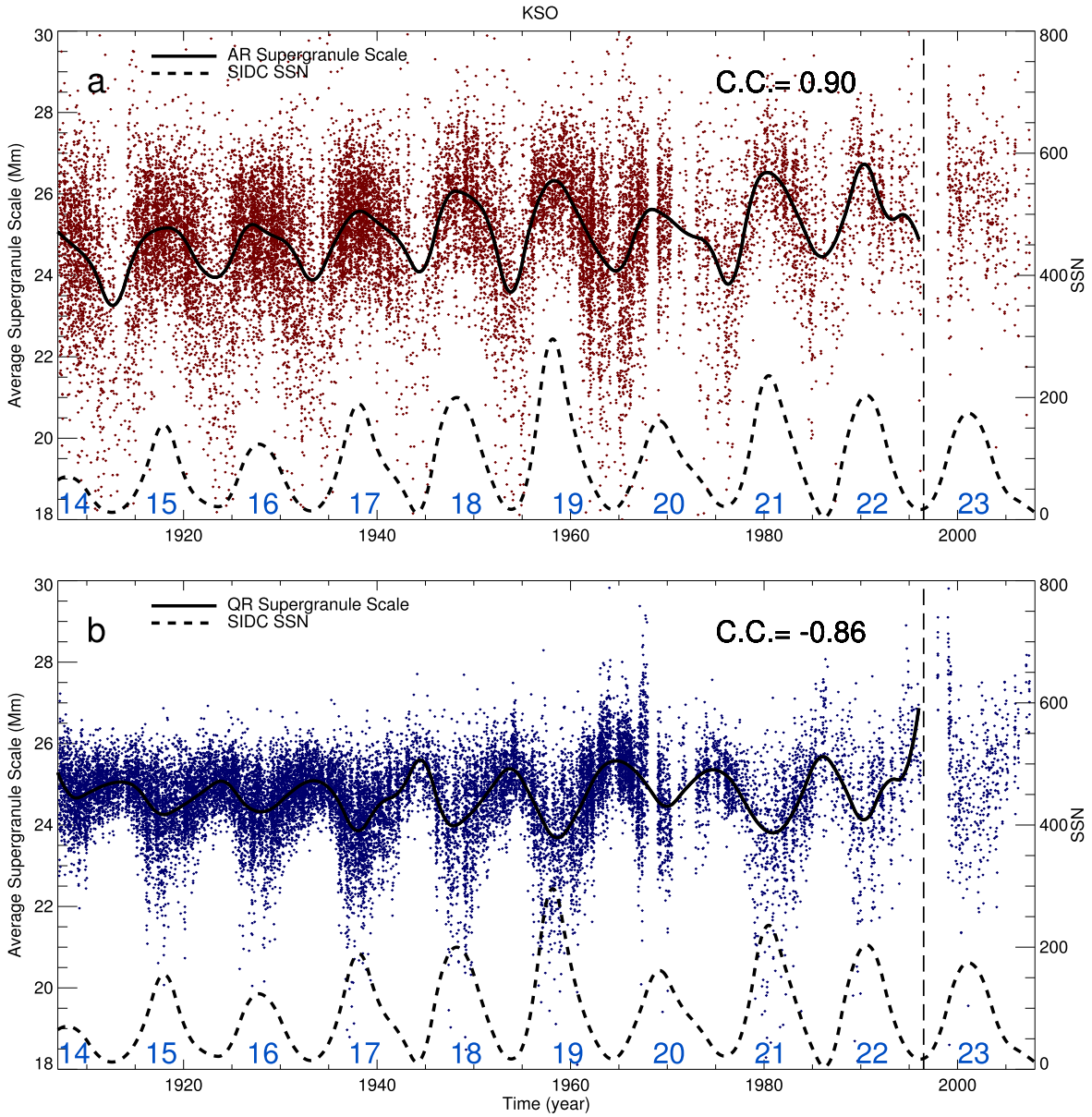

Figure 5. Cyclic variation of mean supergranule scale for the AR (panel a) and for the QR (panel b). Dots correspond to the measured mean scale values from individual images, whereas the solid curves represent the smoothed versions of the same. The SSN cycle is shown with a dashed curve. Individual cycle numbers are marked in blue. The color theme, i.e., results from ARs in red and results from QRs in blue, is followed throughout this paper.

effect of the same on the different properties of supergranules in ARs and on the rest of the Sun, the quite regions (QRs).

Although there have been attempts to divide the solar images into ARs and QRs and study the changes in supergranule scale, all of them were for a very short span of time, at most for one solar cycle (Muenzer et al. 1989; Berrilli et al. 1999; Meunier et al. 2008). In this study we recorded the supergranule parameters separately for AR and QR for more than nine cycles with a fully automated method. To identify the locations of the ARs from the Ca II K images, we used the plage locations as proxies for the magnetic field (Sheeley et al. 2011). All the full-disk limb-darkening-corrected KSO Ca II K images were used to detect plages with a fully automated method, as described in Chatterjee et al. (2016). Next we used a rectangular mask around each of the detected plages with sides three times the maximum distances of plage structure coordinates from the centroids along X and Y. We define these rectangular regions as ARs. This procedure is shown for a representative KSO image in Figure 4(a). We keep a margin of 0.5 times of these X and Y distances, and the region beyond this margin is considered as a QR (Figure 4(b)). The supergranule detection was performed within a rectangular region about the disk center, as shown in Figures 1, 4.

Figure 5 shows the temporal variation of AR and QR supergranule scales with solar cycles. The AR supergranular scale varies coherently with the SSN (plotted as the black dashed curve). The correlation coefficient between the two equals 0.90. In addition to this in-phase variation with the sunspot cycle, we note that the average AR scale in this case is around 25 Mm (we obtained a similar number from the aggregate case, as shown in Figure 3). The temporal variation of the QR supergranule average scale is illustrated in Figure 5(b). Interestingly, for the QR case we find a strong anticorrelation between the mean scale and the SSN cycle. The correlation coefficient is −0.86. For both

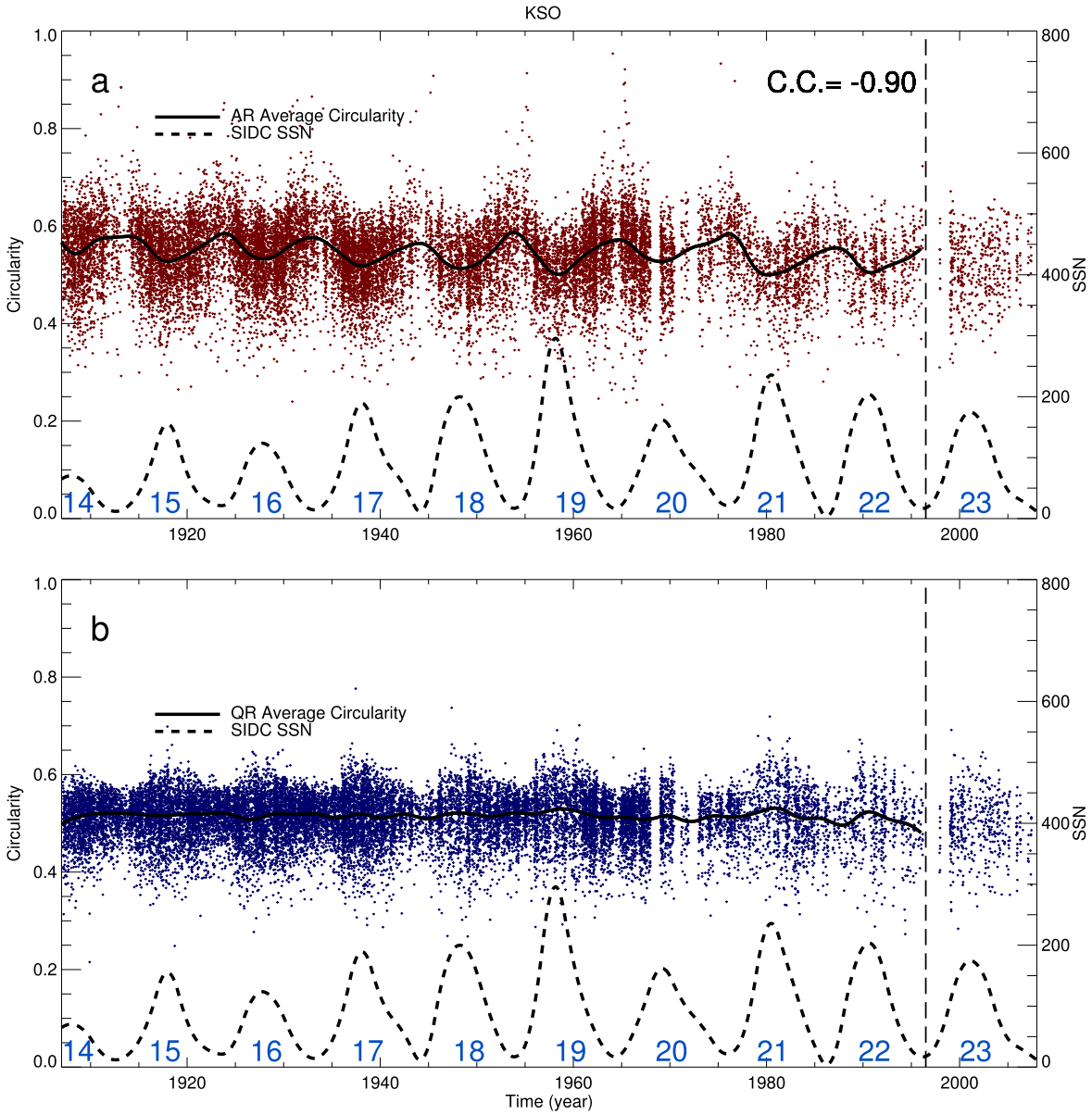

Figure 6. Variation of supergranule circularity for over a century for ARs (panel a) and for QRs (panel b). Dots correspond to circularity values obtained from individual images, whereas the solid curves represent their smoothed version. The SSN cycle is also plotted at the bottom of each panel.

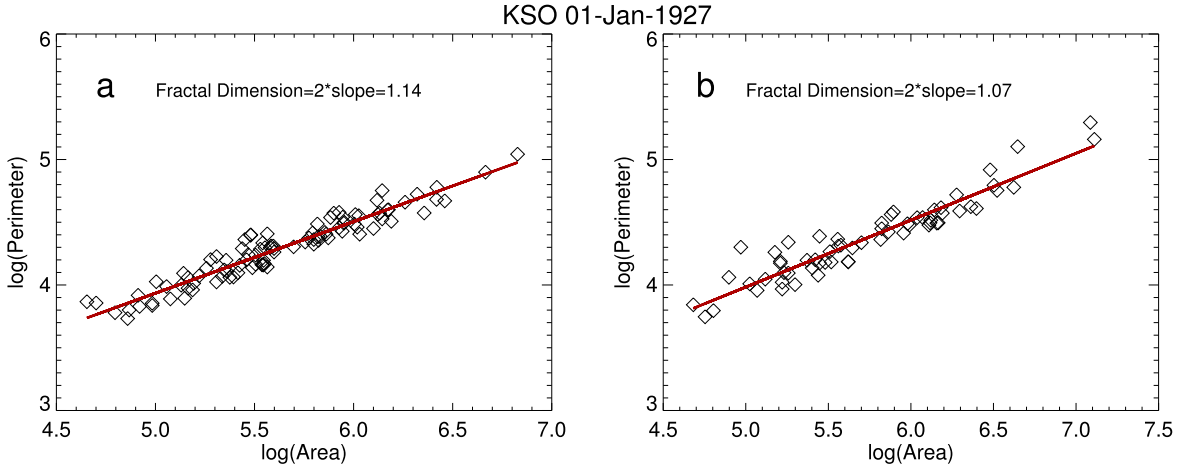

Figure 7. Calculation of the fractal dimension of supergranules. (a) Fractal dimension of supergranules in QRs; (b) fractal dimension of supergranules in ARs.

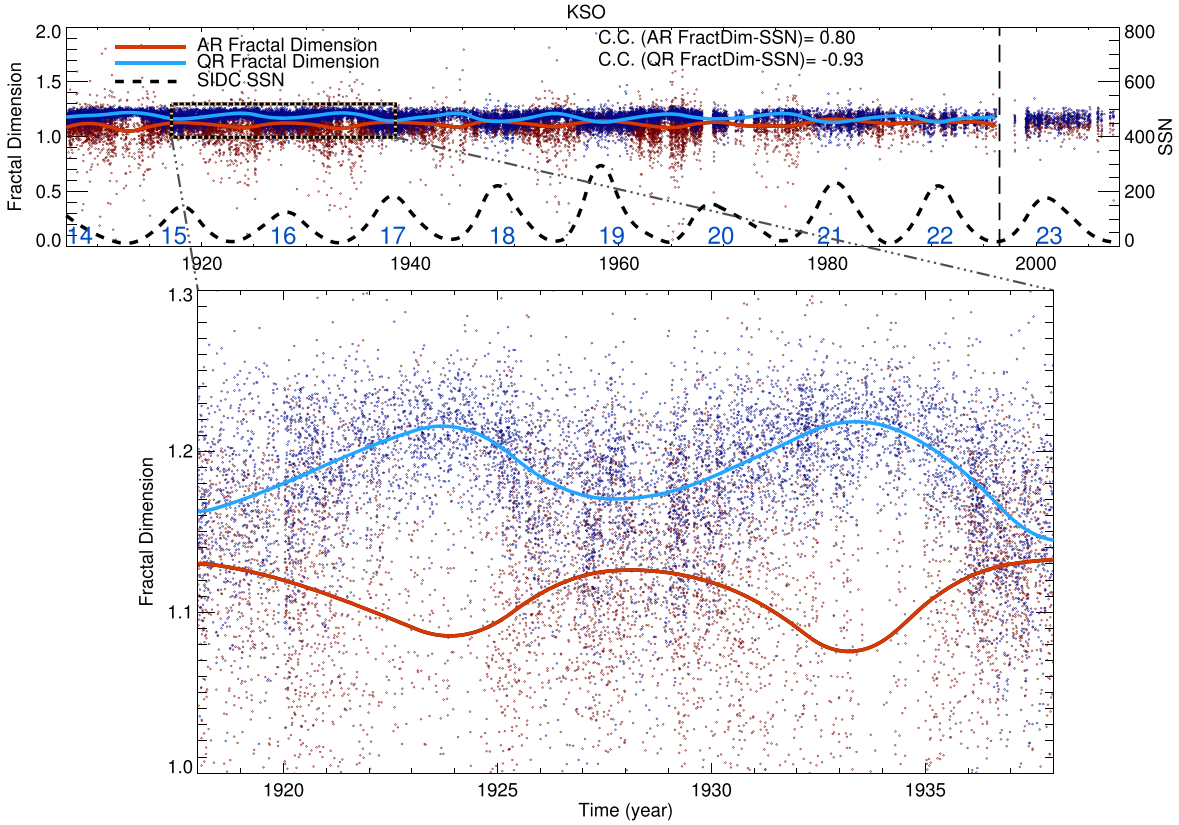

Figure 8. Variation of supergranule fractal dimensions corresponding to individual images in ARs (red dots) and QRs (blue dots). Smoothed curves for the two are shown as solid red and pale blue curves, respectively. The bottom panel presents a magnified view of the region enclosed by the dotted rectangle in the top panel.

the AR and the QR, we find substantial cases when the scale values have comparatively low numbers (≈22 Mm).

We also calculated the scale-normalized average circularity separately for AR and QR, and the results are shown in panels a and b of Figure 6, respectively. From the evolution of the AR circularity, we observe that the supergranules are more circular during the solar minima than during solar maxima. A correlation coefficient of −0.90 confirms this. For the QR (panel 6(b)), it becomes interesting because the circularity parameter shows no apparent correlation with the sunspot cycle.

Next we calculate the fractal dimension for the ARs and the QRs. As defined in Section 3.2, the fractal dimension is equal to twice the slope of the log-log area versus perimeter plot. The different panels of Figure 7 show the calculation of the fractal dimension for the AR and the QR from a single KSO image. Previously, Paniveni et al. (2010) have quantified the AR and QR fractal dimension of supergranules (identified manually) from KSO Ca II K filtergrams for a period of 1.5 years between 2001 and 2002. In this study we recorded the same for a much longer period and also using a fully automated method.

Figure 8 shows the temporal variation of the fractal dimension for the two regions as obtained from the KSO data. For the AR fractal dimension we observe a good correlation (with correlation coefficient 0.80) with the solar cycle. For the QR, it is exactly opposite, i.e., the QR fractal dimension has a strong anticorrelation (with correlation coefficient −0.93) with the solar cycle. Additionally, we note that the fractal dimension for active regions is lower than for quiet regions on an average, as the smoothed pale blue curve rarely dips below the smoothed red curve (in accordance with Paniveni et al. 2010).

5. Results from PSPT

As mentioned in the previous section, the KSO data quality degraded after 1996, and thus the calculated supergranule parameters have more scatter, fewer data points, and large discontinuities.

We therefore used the same technique (of supergranule detection) on the PSPT-Italy and PSPT-USA images. Results from these data sets are shown in the different panels of Figure 9. From the plot we note that the average supergranule scales from two observatories match well. In fact, they are also close to the value obtained from the KSO data (Figure 3). Upon careful observation of the plot, we find some differences, however. The plot reveals a constant shift in the measured supergranule scale values (≈1 Mm) between the PSPT-Italy and PSPT-USA data. The reason behind this may be that the PSPT-Italy data are available in JPEG format, which introduces some compression in the original image, whereas PSPT-USA data are available in standard astronomical FITS format without any compression.

In panel 9(a) we note that the change in the mean scale value from PSPT-Italy does not show a clear in-phase variation with cycle 23 (1996–2008). In the next cycle, cycle 24 (2008 onward), the solar-cycle-like variation resumes. For PSPT-USA (panels 9(b)), we do find an in-phase variation of the same with solar cycle. Thus we conclude that the results from the PSPT-Italy are not due to an detection artifact, but are instead related to the image quality (or continuity) of the telescope.

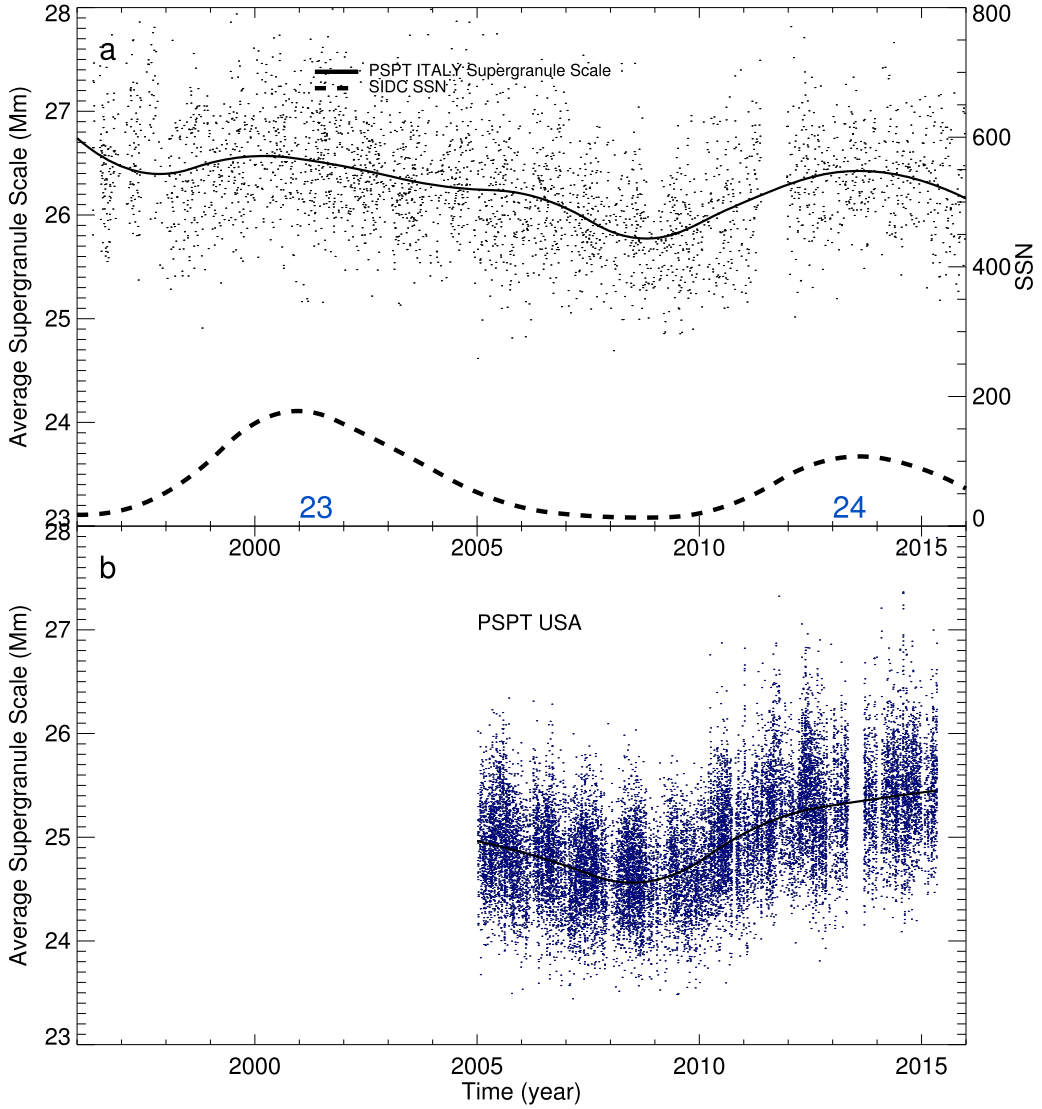

Figure 9. Cyclic variation of the mean supergranule scale for 1996–2016 from various observatories.

6. Summary and Conclusion

In this study, we used for the first time the calibrated Ca II K images recorded at the KSO to identify different supergranule parameters such as mean radius, circularity, and fractal dimension for one century (1907–2007). This has been the longest time series to date for the supergranule geometrical parameters. The main findings are listed below.

1. We implemented a fully automated algorithm to detect the supergranules from the intensity images. Using this automated segmentation method, we find the mean supergranule scale to vary between a range of 22–28 Mm, which is similar to the scale presented in McIntosh et al. (2011).
2. To isolate the effect of the strong large-scale magnetic field on the derived supergranule parameters, we segregate the ARs and QRs from every intensity image using the plages as proxies for the magnetic locations. Analysis shows that the AR supergranule mean scale varies in phase with the solar cycle, whereas for the QR supergranule mean scale it is the opposite. The AR supergranule scale fluctuation about the mean is more than that of the QR values. This means that although the QR scale is anticorrelated with the SSN, the AR scale dominates and causes the aggregate scale to be in phase with the SSN. We conjecture that the AR scale fluctuation is influenced by the spatial extent of magnetic field. It other words, larger ARs during solar maxima might be causing the AR supergranules to become larger. Network magnetic elements have a shrinking effect on supergranules, as hinted by Meunier et al. (2008). During minima they are reduced and might cause larger QR supergranules.
3. The circularity parameter is found to behave differently for the two regions (ARs and QRs). The AR circularity shows a strong anticorrelation with sunspot cycle, whereas the QR circularity shows no dependence. The random walk associated with network magnetic elements might cause the AR supergranules to distort and become less circular during cycle maxima.
4. Fractal dimension, the measure of the boundary irregularity, also has a different and non-overlapping evolution

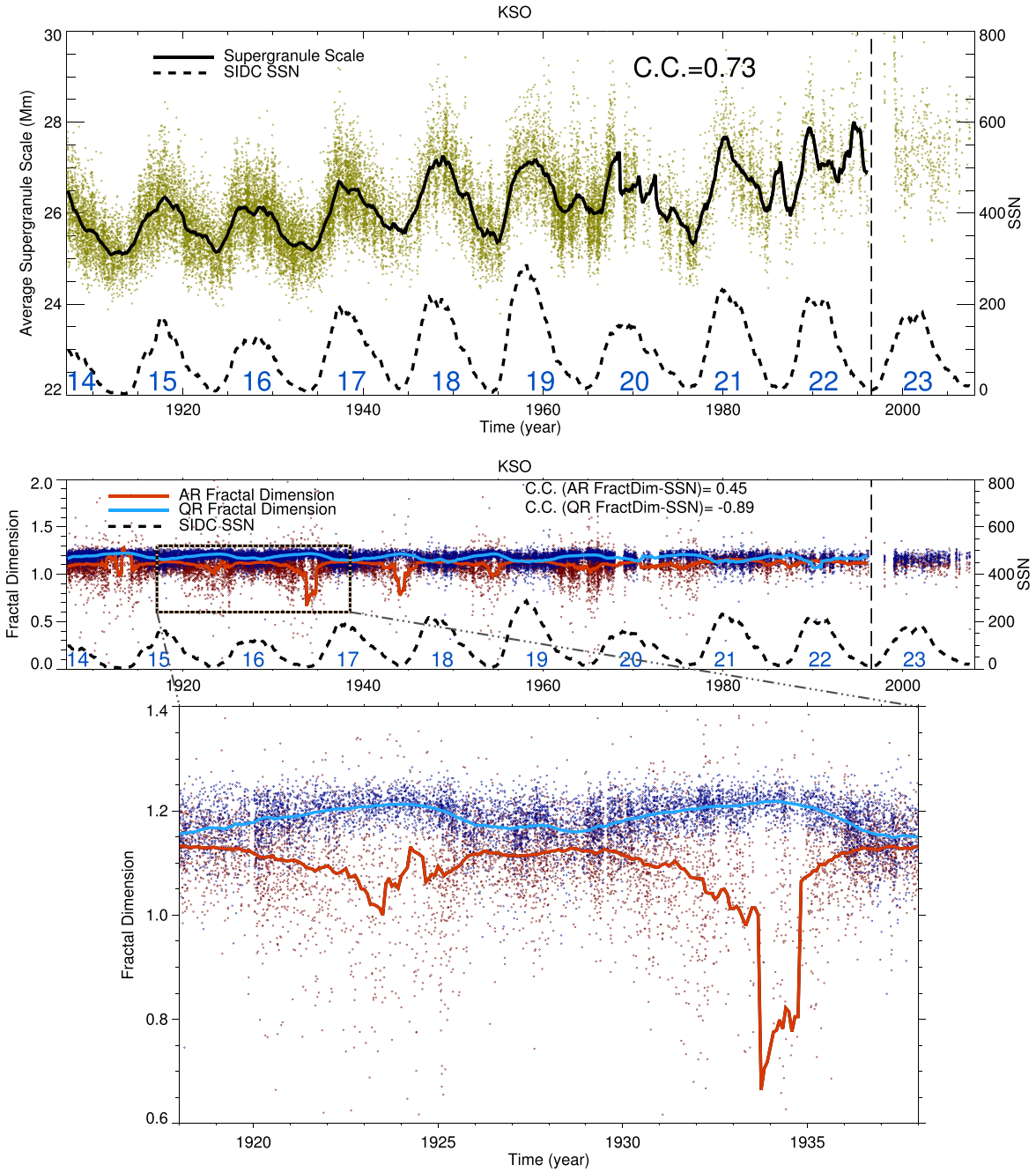

Figure 10. Cyclic variation of supergranule parameters for nine cycles. The upper panel shows the aggregate scale variation and the bottom panel shows the cyclic variation of the fractal dimension for AR and QR. These figures are same as Figures 3 and 8 except that the smoothing approach now is the running average.

for the two regions. In this case, the AR fractal dimension has a positive correlation with the sunspot cycle, whereas the QR has a negative correlation.

5. We also used our detection technique on different data sets from different observatories. The similar parameter values clearly depict the reliability of the technique we used in this paper.

In conclusion, we used a unique data set to study the variation of the supergranular parameters with solar cycle. The variation of the supergranule parameters also has an effect on the total solar irradiance (McIntosh et al. 2011). In our future work we would like to explore this topic further using data from different observatories. Now, ARs are the locations of strong large-scale magnetic fields (mostly the sunspot fields), which are believed to be generated by the global solar dynamo (Charbonneau 2010), whereas the small-scale quiet-Sun magnetic field is believed to be governed by a local dynamo (Stenflo 2012). The different nature of the correlations for AR and QR supergranules thus reflects this inherent difference in the nature of the magnetic fields. It is not clear how the magnetic field influences the scale variability, but our results of segregating the AR and QR provide new constraints that we hope future magneto-convection models will be able to explain.

We would like to thank the Kodaikanal facility of the Indian Institute of Astrophysics, Bangalore, India, for providing the

Table 2
Comparison of Correlation Coefficients (C.C.) for Two Different Smoothing Techniques

Correlated Data Pair	C.C.	
	Running Average	Spline Smoothing
SSN–Aggregate scale	0.73	0.76
SSN–AR scale	0.86	0.90
SSN–QR scale	−0.81	−0.86
SSN–AR circularity	−0.82	−0.90
SSN–AR fractal dimension	0.45	0.80
SSN–QR fractal dimension	−0.89	−0.93

data. These data are now available for public use at https://kso.iiap.res.in/data. We also thank the SCIENCE & ENGINEERING RESEARCH BOARD (SERB) for the project grant (EMR/2014/000626).

Appendix

As mentioned earlier, we recomputed all the correlation coefficients with running-averaged curves in order to verify the reliability of the obtained results. Two of these plots are shown in Figure 10. The top and bottom panels in this plot are similar to Figures 3 and 8 with the smoothing technique being the running average. Comparing the respective plots, we observe that the running average generates a much more jittery curve than the spline-smoothed curves. These jitters result in slightly lower correlation coefficient (C.C.) values. However, the improvements in correlations are mostly marginal except for one case (SSN versus AR fractal dimension). The C.C.s obtained from these two methods are listed in Table 2. Thus, the closeness of the correlation values confirm the fact that the physical interpretations are not affected by the smoothing methods.

References

Berrilli, F., Ermolli, I., Florio, A., & Pietropaolo, E. 1999, A&A, 344, 965
Charbonneau, P. 2010, LRSP, 7, 3
Chatterjee, S., Banerjee, D., & Ravindra, B. 2016, ApJ, 827, 87
Crouch, A. D., Charbonneau, P., & Thibault, K. 2007, ApJ, 662, 715
Ermolli, I., Fofi, M., Bernacchia, C., et al. 1998, in The Prototype RISE-PSPT Instrument Operating in Rome, ed. J. M. Pap, C. Fröhlich, & R. K. Ulrich (Springer Netherlands: Dordrecht), 1
Feigelson, E., & Babu, G. 2012, Modern Statistical Methods for Astronomy: With R Applications (Cambridge: Cambridge Univ. Press)
Hagenaar, H. J., Schrijver, C. J., & Title, A. M. 1997, ApJ, 481, 988
Hastie, T., & Tibshirani, R. 1990, Generalized Additive Models, Chapman & Hall/CRC Monographs on Statistics & Applied Probability (London: Taylor and Francis)
Lin, G., Adiga, U., Olson, K., et al. 2003, Cytometry Part A, 56A, 23
Mandelbrot, B. 1982, The Fractal Geometry of Nature (New York: W. H. Freeman and Company)
McIntosh, S. W., Leamon, R. J., Hock, R. A., Rast, M. P., & Ulrich, R. K. 2011, ApJL, 730, L3
Meunier, N., Roudier, T., & Rieutord, M. 2008, A&A, 488, 1109
Muenzer, H., Schroeter, E. H., Woehl, H., & Hanslmeier, A. 1989, A&A, 213, 431
Muller, R., & Roudier, T. 1994, SoPh, 152, 131
Paniveni, U., Krishan, V., Singh, J., & Srikanth, R. 2010, MNRAS, 402, 424
Priyal, M., Singh, J., Ravindra, B., Priya, T. G., & Amareswari, K. 2014, SoPh, 289, 137
Rast, M. P. 2003, ApJ, 597, 1200
Reinsch, C. H. 1967, NuMat, 10, 177
Rieutord, M., & Rincon, F. 2010, LRSP, 7, 2
Sheeley, N. R., Jr., Cooper, T. J., & Anderson, J. R. L. 2011, ApJ, 730, 51
Simon, G. W., & Leighton, R. B. 1964, ApJ, 140, 1120
Sonka, M., Hlavac, V., & Boyle, R. 2014, Image Processing, Analysis, and Machine Vision (Andover: Cengage Learning)
Srikanth, R., Singh, J., & Raju, K. P. 2000, ApJ, 534, 1008
Stenflo, J. O. 2012, A&A, 547, A93
Sýkora, J. 1970, SoPh, 13, 292
Vincent, L., & Soille, P. 1991, ITPAM, 13, 583